Medical Applications of Accelerated Ions

Wilma K. Weyrather

Gesellschaft für Schwerionenforschung, Planckstr. 1, 64291 Darmstadt, Germany

Abstract. Accelerated ions have significant advantages for radiotherapy. From the physical side these are the inverse depth dose profile (the increase of the dose with penetration depth) and the finite range defined by the energy. Both factors, together with a small lateral scattering, provide an optimal dose distribution that makes ions an ideal tool for the treatment of deep-seated tumors close to radiosensitive organs. For carbon ions the positive physical dose distribution is potentiated by the increased relative biological effectiveness (RBE) towards the end of the particle range, which offers an additional advantage for slow growing radioresistent tumors. To exploit the high RBE to a maximum, a strict tumor conform dose application is necessary. Therefore, an active beam delivery system with an intensity-controlled rasterscan as well as a biologically optimized treatment planning based on the local effect model (LEM) have been developed at GSI. Positron emitters like ^{10}C, ^{11}C and ^{15}O that are produced by the primary beam can be used to monitor the stopping point of the primary beam inside the patient using Positron Emitting Tomograpy (PET) techniques. This lecture reviews the physical and biological basis of the therapy with accelerated ions and introduces the technical and mathematical tools necessary for the realisation. Positive early medical results will encourage the realisation of other planned centres.

1 Introduction

There has rarely been another finding of a physical phenomenon with a similar impact to medicine as Wilhelm Conrad Röntgen's discovery of the X-rays in November 1895. A carefully reasoned description of his work together with the famous radiograph of his wife's hand was published in a short time: 'Eine neue Art von Strahlen'. A reproduction of this publication can be visited at the Röntgen museum at Würzburg. While the implication for medical diagnostic had already immediately been foreseen by Röntgen himself, the idea of a benefit from a use in benign and malignant conditions came up only weeks later. The first successful treatment of a patient, that also gave a scientific proof of the therapeutic effectiveness of X-rays was carried out in late November 1896 by Leopold Freund [1].

But though some negative effects on the skin were soon observed, it took until 1904, when Edison's assistant Clarence Dally died following injuries to his hands and arms [2], that physicians and physicists took the possibly fatal power of the X-rays into account.

W.K. Weyrather, Medical Applications of Accelerated Ions, Lect. Notes Phys. **651**, 469–490 (2004)
http://www.springerlink.com/

In the following decades many efforts were made to overcome the unfavourable exponential dose distribution of X-rays. With the use of Co-γ and lateron photons from electron linacs the dose maximum could be shifted from the sensitive skin to deeper parts. Nowadays sophisticated treatment like IMRT (Intensity modulated radiation therapy) try to optimize the dose distribution and confine it to treat tumors.

The observation of R.E. Zirkle in 1935 who found, after irradiation of plant cells with alpha particles from polonium, that biological effects depend on ionization density [3] and the findings of J.H. Lawrence *et al.*, that the biological effect of neutrons compared to photons was higher on neoplastic tissue than in normal tissue [4] were the rationale for using neutrons in radiotherapy. The early encouraging results with effective tumor response were later followed by drastic late effects like necrotic normal tissue [5]. The higher efficiency of the high LET that was favorable especially for radioresistant and often partially hypoxic tumors, led also to drastic damage in the normal tissue. This is due to the exponential depth dose profile that, as in the case of photons, delivers the highest dose to the skin.

The first person to suggest a way of overcoming this problem was Robert Wilson in 1946 [6]. He proposed the application of protons, that promised a much better dose distribution. Two years later this was tested at the 184-inch cyclotron at Berkeley by Tobias and his colleagues [7]. The first clinical use of protons was in 1954 in Berkeley [8], and was soon followed at Uppsala and Harvard. In the meantime more than thirty thousand patients worldwide have been treated with protons.

As protons show mainly a biological effectiveness similar to photons, the use of heavier ions was the next logical step, as already suggested by C.A.Tobias in the 1950s. Heavier particles combine the more favorable dose distribution of the protons and the benefit from the high LET. It has been a long journey from the irradiation of the first patient in 1975 in Berkeley to the present state. The irradiation technique had to be optimized to be able to restrict the high LET radiation strictly to the tumor volume, and much research has been done to learn how to use this enhanced biological efficiency to an optimum.

2 The Physical Basis of Ion Beam Therapy

2.1 Depth Dose Distribution of Photons

In the interaction of electromagnetic radiation with matter the energy loss is mainly due to three processes (Fig. 1)

1. Photoelectric effect
2. Compton scattering
3. Electron-positron pair production

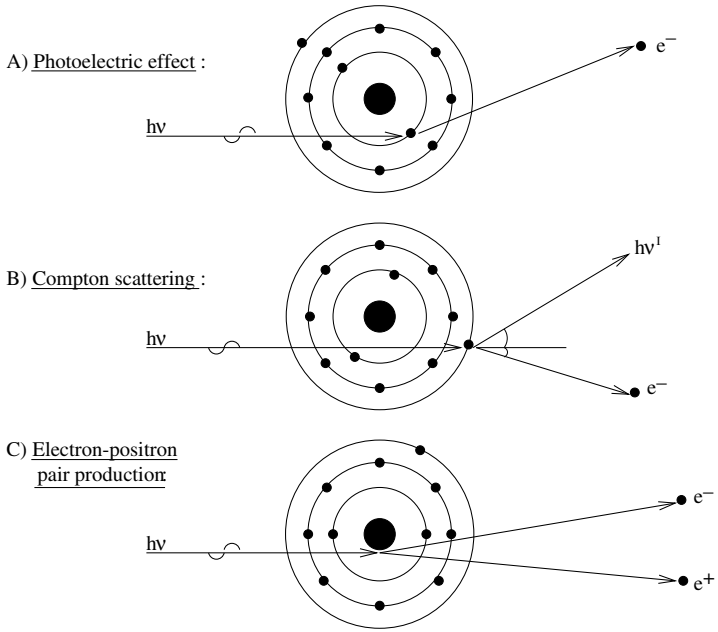

Fig. 1. Absorption of photons by (**a)** photoelectric effect: the energy of the photon is totally absorbed by the atom, ejecting a tightly bound orbital electron with the kinetic energy that is equal to the difference of photon energy and the electron binding energy, (**b)** Compton scattering: the photon interacts with a loosely bound electron, which takes only part of the photon energy as kinetic energy. The deflected photon proceeds with reduced energy. (**c)** electron-positron pair production: at photon energies much above 1 MeV the photon energy is converted in the field of the nucleus into an electron-positron pair.

The relative probability of one of these interactions occurring is a function of the incident photon energy and the atomic number Z of the absorbing material. For low energy X-rays the stochastic absorption by photo and Compton processes yields an exponential decay of the absorbed dose with penetration depth according to

$$I = I_0 e^{-\mu d} \tag{1}$$

where I_0 is the initial energy and μ the attenuation coefficient. Higher photon energies like Co-γ-radiation cause strong forward scattering of the produced Compton electrons, which results in an increased dose within the first few centimeters. Figure 2 shows the depth dose profile of electromagnetic radiation for different energies. For high energy electron Bremsstrahlung, that is mostly used in modern conventional therapy, the maximum is shifted to a few centimeters from surface and the exponential decay is less steep. This shift of the dose maximum and the less steep descent of the dose distribution

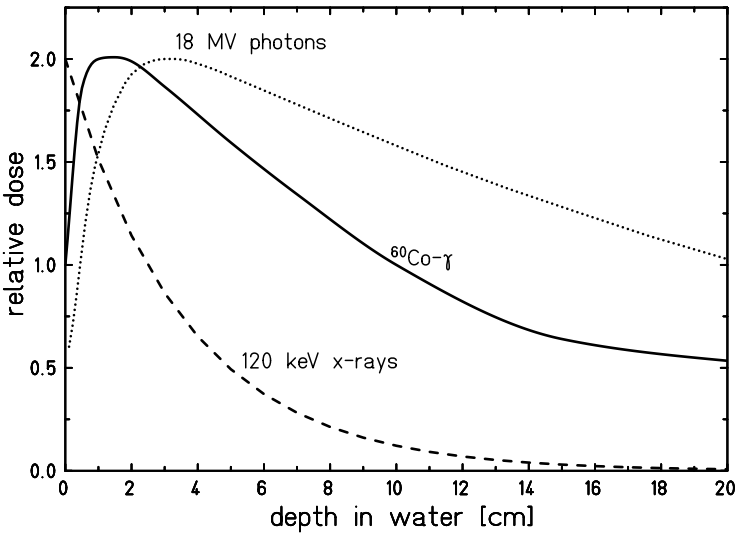

Fig. 2. Depth dose profiles of x-rays, Co-gamma and Röntgen-Bremsstrahlung (with courtesy of U.Weber).

with penetration depth is the main reason for the transition to high energy photons from electron linacs presently used in most hospitals.

2.2 Inverse Dose Distribution of Ions

The most prominent feature of accelerated ions for their use in radiation therapy is the inversed dose profile. The increased energy deposition with penetration depth up to a sharp maximum at the end of the particle range was first measured by William Bragg with alpha particles in air [9], and this maximum is known as the Bragg peak.

The energy of the ions is mostly transferred to the target electrons that are emitted as delta electrons (Fig. 3). More than three quarters of the dissipated energy is used for the ionisation process and only 10 to 20% for target atom excitation [10]. The interaction strength is directly correlated with the interaction time. At high energies, when the interaction time is short, the energy transfer to the target is small but grows when the particles are slowed down (according to a $\frac{1}{v^2}$ law).

The macroscopic dose of a particle beam is given by the number of particles traversing the unit mass and the dose deposited by each particle, called linear energy transfer (LET). This energy deposition of heavy charged particles, like protons or heavier ions (Fig. 4), can be decribed by the Bethe-Bloch-formula [11–13]

$$-\frac{dE}{dx} = \frac{4\pi e^4 Z_{eff}^2 ZN}{m_e v^2} ln \frac{2mv^2}{I} + \textit{relativistic terms} \ , \qquad (2)$$

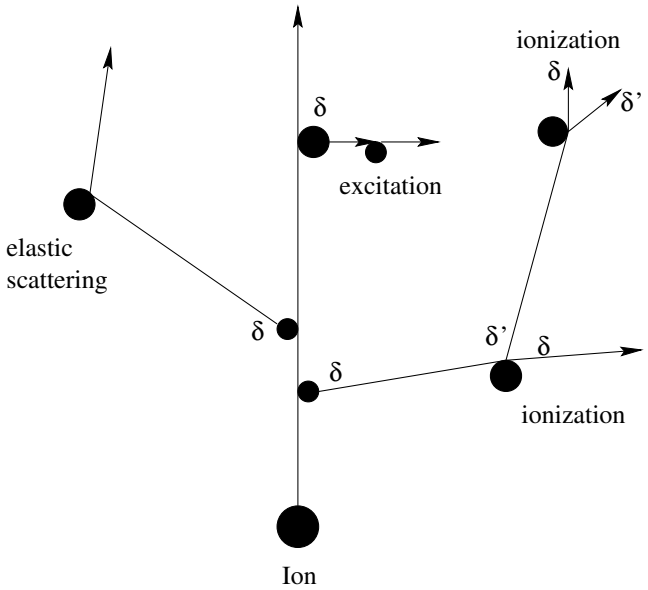

Fig. 3. The energy of the projectile is transferred in fractions to the target electrons, that are emitted as delta electrons. High energy delta electrons can cause secondary ionisation and form individual short tracks, called delta rays (with courtesy of M. Krämer).

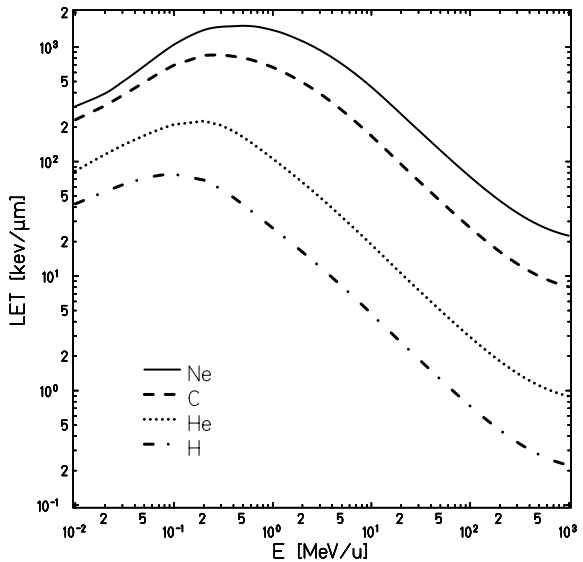

Fig. 4. Energy loss of different particles as function of the energy (calculated with ATIMA [15]).

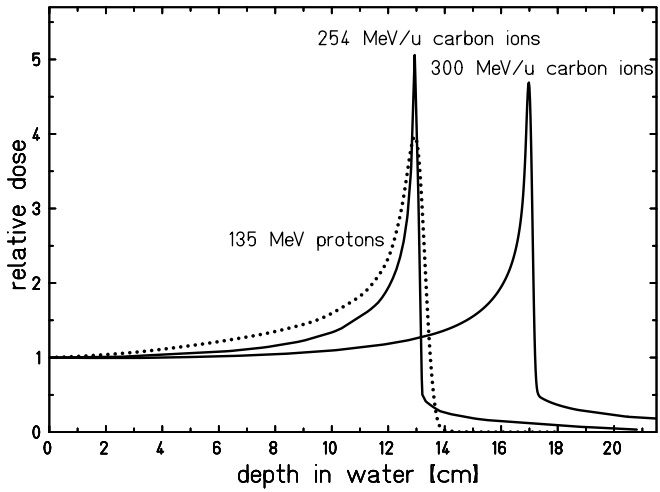

Fig. 5. Depth dose distribution for carbon ions of 254 MeV/u and 300 MeV/u and 135 MeV protons (with courtesy of U.Weber).

with $\frac{dE}{dx}$ being the energy loss per length, Z the target atomic number, N the electron density of the target, m_e and e the mass and the charge of the electron, $v = \beta c$ the projectile velocity and Z_{eff} the effective projectile charge, which can be approximated by the Barkas formula [14]

$$Z_{eff} = Z(1 - e^{-125\beta Z^{-\frac{2}{3}}}) \; . \tag{3}$$

The $\frac{1}{v^2}$ dependence leads to an increase in energy loss with decreasing energy. At low energies electrons are collected from the target and Z_{eff} decreases rapidly. This leads to the maximum of energy loss between 0.1 and 1 MeV as shown in Fig. 4. When Z_{eff} goes to zero, the energy loss goes to zero, too, causing a finite range of the particle. A plot versus the penetration depth shows, that this maximum energy loss is located at the very end of the particle range (Bragg-peak), whereas the low energy loss at high energies yields a nearly constant plateau in the entrance channel (Fig. 5). The width of the Bragg-peak is due to multiple scattering processes, that yield an almost Gaussian energy loss distribution [16,17]. Because these processes strongly depend on the atomic number of the projectile, the resulting range straggling is more pronounced for the lighter protons than for the carbon ions.

2.3 Lateral Scattering

The lateral scattering mainly results from the Coulomb interaction of the projectiles with the target nuclei, which is decribed in the theory of Moliere [18]. Figure 6 shows the calculated beam broadening for protons, helium, carbon

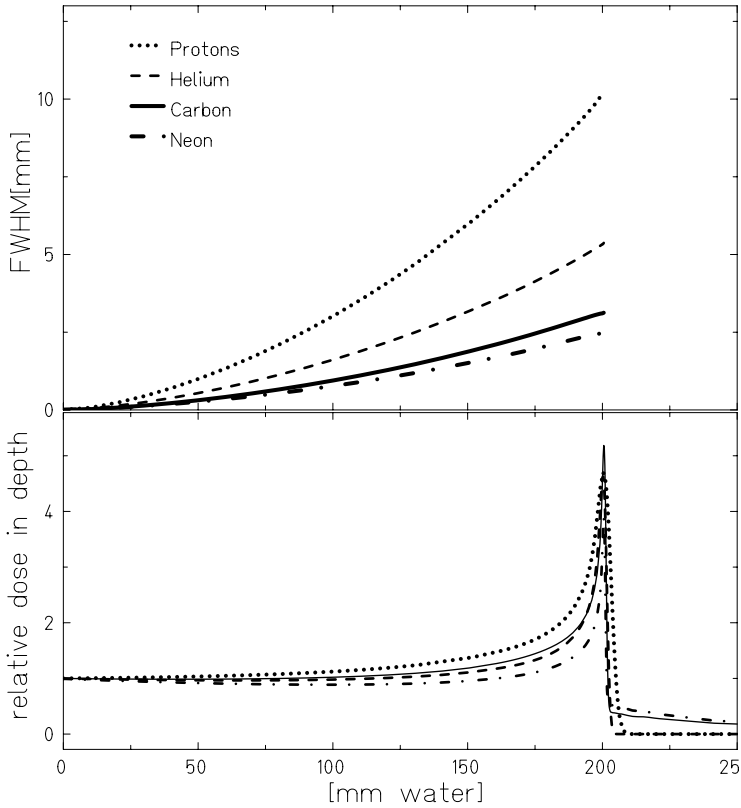

Fig. 6. Comparison of the lateral scattering for different particles (top) and depth dose distribution for equal particle range (bottom) (Calculated with the 'scatter' and 'yield' components of TRiP98 [43]

and neon. There is a big difference between protons and helium ions whereas a change from carbon to neon ions gives only marginal further improvements. A small part of the lateral beam is also due to the kinematics of nuclear reactions (see next chapter) especially at the distal part of the Bragg peak where only nuclear fragments contribute to the dose. In radiotherapy the term 'distal' is used for the more distant part from the radiation source i.e. from the accelerator. The opposite part is called 'proximal'.

2.4 Nuclear Fragmentation

When an energetic particle beam passes through tissue or other material, nuclear reactions take place which cause a small amount nuclear fragmentation. The result is a reduced number of primary particles that reach the tumor but replaced by a number of secondary and tertiary fragments. Most of the lighter fragments have the same velocity as the primary ions at the

collision [19]. The range of these fragments is given by the formula:

$$R_{fr} = R_{pr} \frac{Z_{pr}^2 M_{fr}}{M_{pr} Z_{fr}^2} \ , \tag{4}$$

with R being the range, Z the atomic number and M the masses of the fragments (subscripts *fr*) and the projectiles (subscript *pr*), respectively. According to this equation the lighter fragments have a longer range than the primary particles and are responsible for the undesired dose behind the Bragg-peak. On the other hand, radioactive positron-emitting isotopes, which are also produced in these processes are very useful to track the beam path inside the patient (See Sect. 4.4).

3 The Enhanced Relative Biological Effectiveness (RBE)

The most important effect for tumor therapy is the biological action of the ions. In general the biological efficiency increases for heavier ions but the efficiency of particle beams to induce biological damage changes along their path.

3.1 Molecular Mechanisms Yielding Increased RBE

The changes in the biological effectiveness are the result of a complex interplay between physical parameters like ionisation density and biological parameters, mainly the repair capacity of the cell system.

Sparsely ionising radiation like photons and X-rays produces damage in a stochastic manner, where the dose is distributed randomly throughout the cell. This is schematically explained in Fig. 7. Low doses lead from the undamaged double stranded DNA (A) first to separated single strand breaks and single base damages (B) which can mostly be repaired. Two single strand breaks occuring close enough together may lead to a double strand break (C), which in most cases can also be repaired by the cell. Only when the local dose becomes high enough that the produced damage cannot be sufficiently repaired will a lethal event result (D). Therefore, the biological response for sparsely ionising radiation is a non-linear function and can be approximated by a linear quadratic expression

$$S = S_0 exp(-\alpha D - \beta D^2) \ , \tag{5}$$

where S is the survival, D the dose and α and β are specific coefficients, characterizing the radiation response. A plot of the survival in a semi-logarithmic scale leads to the characteristic shouldered survival curve (Fig. 8, curve (1)), with the size of the shoulder being a measure of the repair capacity of the cell or tissue.

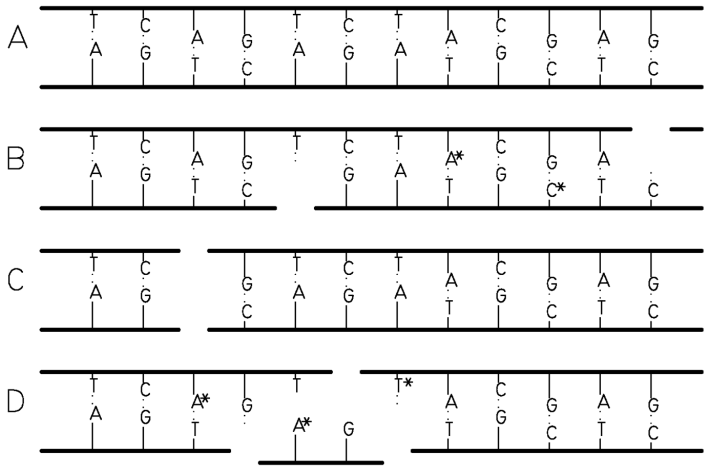

Fig. 7. Schematic view of an undamaged part of DNA (**A**), two separated single strand breaks (**B**), a double strand break (**C**), and a 'clustered lesion' (**D**). The (*) indicate a base damage.

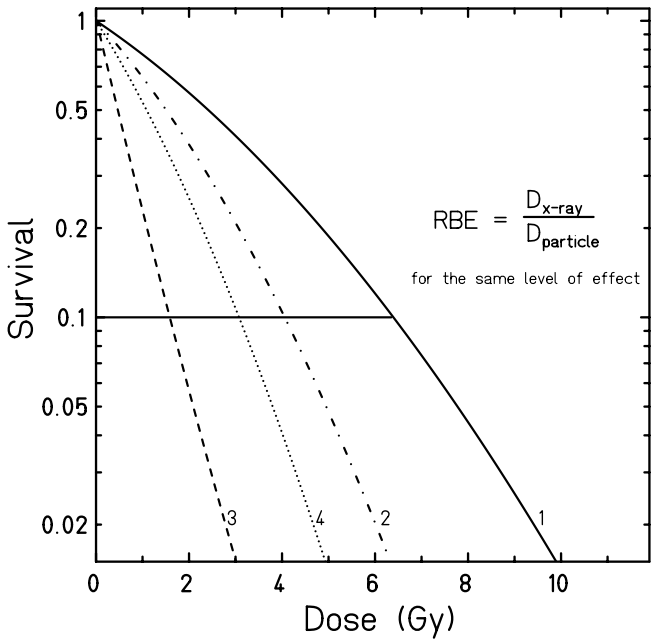

Fig. 8. Survival curves for CHO-K1 cells irradiated with x-rays [**1**] and carbon ions of different energies: [**2**] 266.4 MeV/u LET=13.7keV/μm, [**3**] 11.0 MeV/u LET=153.0keV/μm, [**4**] 2.4 MeV/u LET=482.7keV/μm

For particles, the ionisation occurs along the trajectory of the ion and most of the energy loss is transferred to the liberated electrons, which form a track around the particle trajectory. The diameter of the track depends on the range of the electrons and, thus, the velocity of the ion, independent of the atomic number, whereas the deposited energy in terms of LET (linear energy transfer) depends on the atomic number squared, and on the velocity. In a high LET track the damage is produced in high density and consequently as 'clustered lesions' that are, to a large amount, irreparable. This leads to purely exponential curves with β approaching 0 (Fig. 8, curve (3)). This different action of sparsely and densely ionising radiation is quantitatively described in terms of the *Relative Biological Effectiveness* (RBE), which compares the dose of densely ionizing radiation to the dose of sparsely ionizing radiation (mostly 220 keV X-rays [20]) producing the same biological effect

$$\mathrm{RBE} = \frac{D_{X-ray}}{D_{particle}} \ . \tag{6}$$

Because RBE refers to the linear quadratic X-ray dose effect curve, RBE strongly depends on effect level: it is high for low doses and decreases with increasing dose. Thus the effect level has to be always given as an index with the RBE level. The ratio of the α-terms as the initial slope of the dose effect curve defines the maximum value RBE_{α}. For comparison, the value at the 10% survival level RBE_{10} is often used in the literature. Increasing local ionisation density has been shown experimentally in the induction of DNA double strand breaks [21] and made visible in immunfluorescence-stained cells by measuring the response of repair and signalling proteins to high LET irradiation [22].

3.2 RBE and Energy and Atomic Number of the Particle

Figure 8 shows that different energies of the carbon ions yield different dose-effect curves. Qualitatively, this can be easily explained: For high energies the track is wide and the LET low, thus the ionisation events occur far enough apart to make repair possible, yielding shouldered curves similar to sparsely ionising radiation. With decreasing energy the diameter of the track shrinks and the LET increases. This leads to a high ionisation density where the ionisation events occur closely together with a high possibility of interaction, diminishing the influence of repair and yielding a significantly increased RBE. At very high LET values at the end of the particle range (for carbon ions this is above 200 keV/μm) the local dose density becomes higher than necessary for a lethal damage and RBE decreases again. This is shown in Fig. 9 converted into a depth distribution in water.

The dependence of RBE on LET is different for different ions, showing a separate maximum for each atomic number shifting from 25 keV/μm for protons [23,24] to higher LET values for heavier ions [25,26]. In addition, the difference between minimal and maximal RBE is greater for lighter ions.

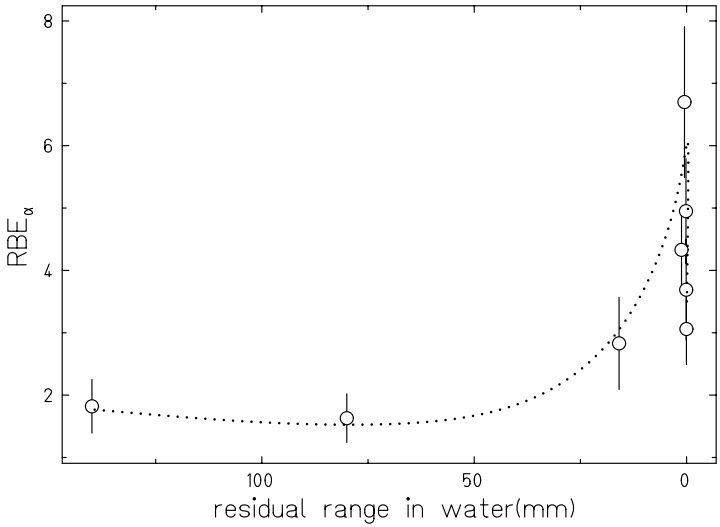

Fig. 9. RBE_α for carbon irradiated CHO-K1 cells. Data from [28]

For carbon ions the RBE maximum overlaps with the Bragg peak. Therefore the high RBE is preserved also in an extended volume.

For protons this is different. As the spatial distribution of the ionisation density in the proton beam is very high only at the distal end of the Bragg peak, i.e. at the very end of the range, the ionisation density is mixed and washed out by the range straggling in the case of a spread-out Bragg peak. This leads to a partial levelling of the RBE in a modulated Bragg peak, having a high RBE only at the distal end. As the range straggling depends on the energy, the levelling of the proton RBE increases with increasing initial proton energy [27].

For ions heavier than oxygen the RBE becomes large in front of the Bragg maximum, already diminishing the difference in RBE between tumor and normal tissue.

3.3 RBE and Repair Capacity of the Irradiated Tissue

As the main difference between sparsely and densely ionising irradiation is the amount of repairable damage produced, RBE depends essentially on the repair capacity of the irradiated tissue. An example is shown in Fig. 10. Two types of Chinese hamster ovary cells CHO-K1 have been exposed to carbon ions of different energies, the repair proficient wild type and the repair deficient mutant xrs-5 [28]. For X-ray irradiation the wild type shows a large shoulder, which is reduced with increasing LET (see Fig. 8). The repair deficient mutant xrs-5 shows no shoulder for X-rays, indicating that there is no repair. Therefore an increased LET has no influence. When cells are al-

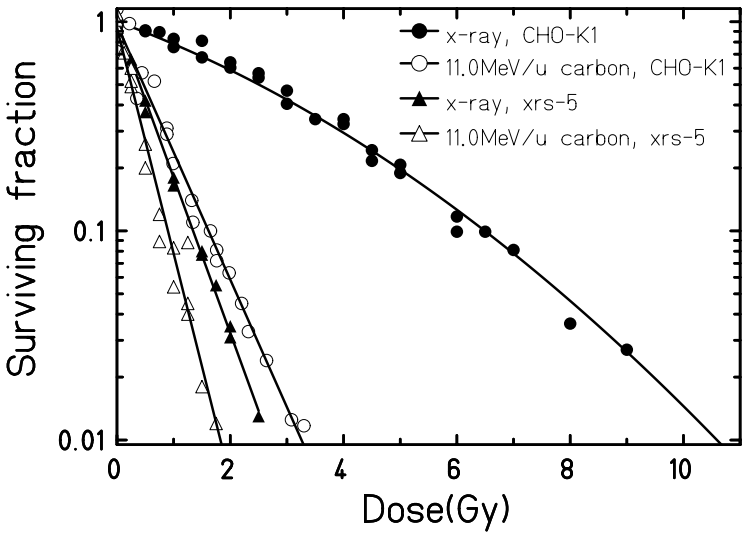

Fig. 10. Cell survival for the repair proficient wild type cell line CHO-K1 and its repair deficient mutant xrs-5. Data from [28]

ready radiosensitive and simple lesions cannot be repaired, an increase in local ionisation density does not result in less repair.

In general the RBE is high for cells and tissues with a high repair capacity, it is lower for repair deficient cells and close to 1 for non-repairing cells [28, 29]. This can be demonstrated in a relation between RBE and the α/β - value of the X-ray curve (Fig. 11). For the same beam and the same tissue or cell type various RBE values may exist for different biological reactions or endpoints due to different pathways of biological reactions in the cell, for example for cell killing and the late effects neoplastic transformation [33] and mutation [34].

A major problem in radiotherapy is the 'oxygen effect', which means that irradiation in the presence of oxygen causes higher biological damage than in the absence of oxygen. The ratio of the doses leading to the same effect in oxic and in hypoxic cells or tissue is called Oxygen Enhancement Ratio (OER). The reaction is mainly caused by radiation induced free radicals, which cause biological damage after a chain of events. In the absence of oxygen most of these ionized target molecules can repair themselves and recover. If oxygen is present, it reacts with the free radical $R^{\bullet}$ to $RO_2^{\bullet}$ and fixes the radiation lesion in this way. This means that the often hypoxic tumors may be up to three times more radioresistent than the well blood-supplied, and therefore oxic, normal tissue [31]. As the damage from high LET particles does not differ for aerobic or anerobic cells, the OER is smaller for heavy stopping particles (carbon and heavier). Thus, RBE is higher for the, generally radioresistant poor, oxygenated tissue [32,35].

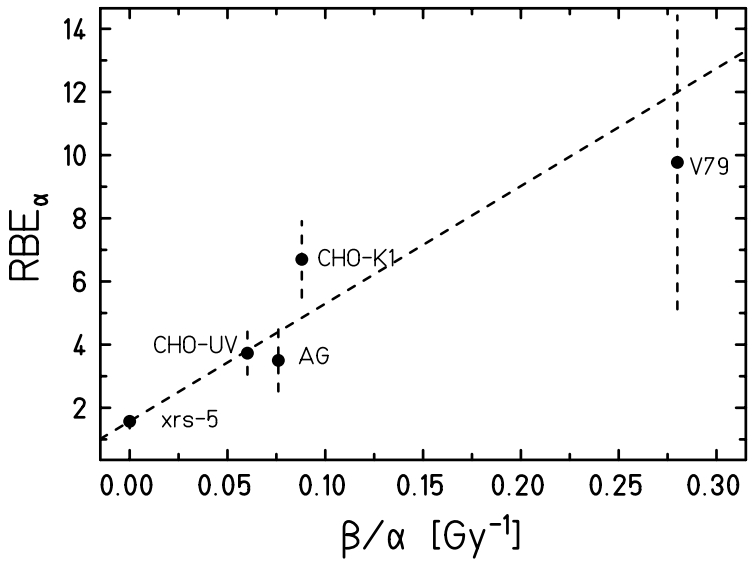

Fig. 11. RBE_α for different cell lines irradiated with 11 MeV/u carbon ions compared to the inversed α/β ratio for X-rays [30]

3.4 RBE Calculation for Therapy

The extremely target conformal irradiation, due to the active beam shaping system, has the consequence that RBE varies over the complete irradiated volume in all three dimensions. In each volume element, a mixture of primary and secondary ions contributes to the dose and this mixture has to be taken into account since RBE depends on atomic number and energy. Therefore, in treatment planning RBE has to be calculated separately for each voxel of the treated volume [36,44]. At GSI, this calculation is done using the Local Effect Model (LEM) [37]. In this model the size of the cell nucleus, the radial dose distribution $D(r)$ inside the particle tracks and the X-ray dose-effect curve $S_x(D)$ are used as basis for the calculation. The principle idea is shown schematically in Fig. 12: the dotted circular area represents the cell nucleus, which is assumed to be the critical target. In a first approximation it can be assumed that the sensitive sites are distributed homogeneously over the cell nucleus. For the calculation the cell nucleus is subdivided into small compartments for each of which the average dose deposition is determined from the corresponding radial dose profiles from the individual tracks. The biological effect in this compartment is then calculated from the effect observed for photon irradiation at the same dose. The total average number of lethal events can then be calculated according to

$$N_{lethal} = \int_x \int_y \int_z \frac{-lnS_x(D(x,y,z))}{V} dxdydz \ , \tag{7}$$

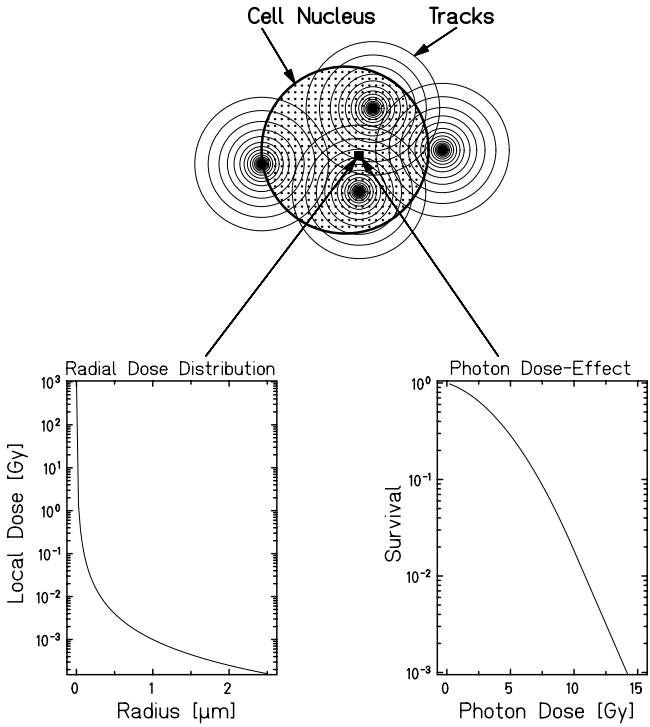

Fig. 12. Principle of the local effect model (With courtesy from M. Scholz)

where S_x is the photon dose response curve, $D(x, y, z)$ the actual local dose at the point (x, y, z) in the cell nucleus and V is the volume of the cell nucleus [40].

The survival probability for an individual cell after ion exposure is

$$S_{ion} = e^{-N_{lethal}} \ . \tag{8}$$

From the average survival determined from an appropriate number of cells, RBE values are derived for the average dose deposited in a given voxel. Thus the RBE is calculated for each volume element separately, yielding a map of RBE values over the complete irradiated volume. The model can be applied to biological endpoints in-vitro and in-vivo [38] [39]. For therapy planning this X-ray sensitivity is not deduced from in-vitro experiments. Instead, the known X-ray sensitivity of the same tumor histology – or concerning late effects of the irradiated normal tissue – is used as the basis for the calculations.

4 Tumorconform Treatment

4.1 Active Energy Variation

In practical use in therapy, the tumor volume to be treated is normally much larger than the width of the Bragg peak and the lateral dimension of the particle beam. In order to fill the target volume with the necessary amount of stopping particles the peak has to be 'spread out'. This can be done in two ways: for the passive energy variation, a fixed energy from the accelerator that is high enough for all required ranges is used. The energy variation is achieved by inserting material in the beam path (either an adjustable water column or range shifters of other material). This is the easiest method when a fast energy variation from the accelerator is not possible. The disadvantages of this method are: a higher amount of projectile fragments, which deliver an unwanted high dose behind the Bragg peak of the primary ion, an enhanced lateral scattering, mainly due the protons and other lighter fragments, and the high RBE part cannot be completely restricted to the tumor volume [41]. In the active energy variation the tumor is dissected into layers of equal particle range and after the irradiation of one layer the energy is adjusted to the next range by the accelerator (in this case a synchrotron). In the most favorable case this can be done pulse by pulse. Here it has to be considered, that this layer has already been partly covered by dose from the irradiation of the more distal layer. In this way an 'extended Bragg peak' can be constructed (Fig. 13).

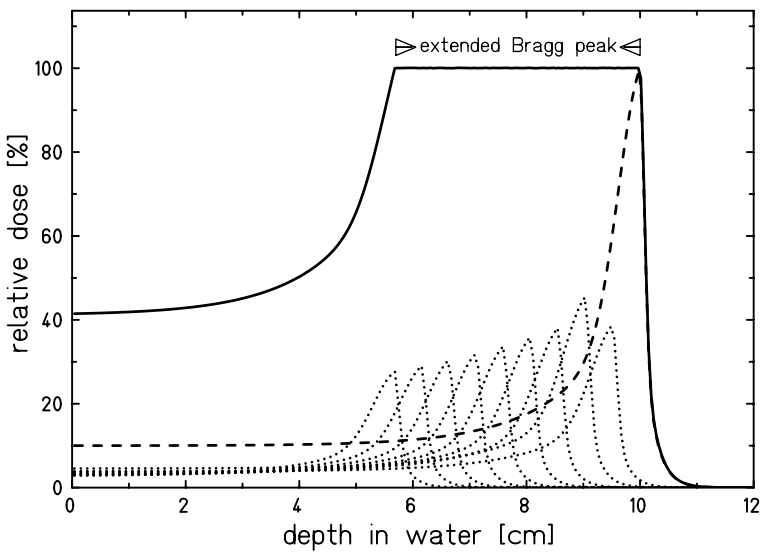

Fig. 13. Construction of an extended Bragg-peak by superposition of single Bragg-peaks of different energy.

4.2 Magnetic Beam Scanning

In active beam-shaping, the lateral adjustment to the tumor volume is done by an intensity controlled magnetic scanning system, that allows the irradiated volume to be conformed to the planned target volume within a millimeter precision. Each layer of equal particle energy is covered by a grid of individual picture elements (pixels), for which the individual number of particles has been calculated before, to achieve the desired dose distribution [42]. The beam is moved from one pixel to the next using a pair of magnets perpendicular to each other and to the beam direction and driven by fast power supplies (Fig. 14).

The particle fluence for each pixel is measured and the beam is switched to the next pixel when the intensity for one position has been reached. Due to the irregular shape of the energy slices, the dose from the irradiation of the more distal layers is different for every pixel. Thus, an inhomogeneous particle distribution is necessary to achieve a homogeneous distribution of the biological effect over the total target volume. The advantage of the active shaping system is the extreme precision. Thus, a tumor adjacent to critical organs like brain stem or optical nerves can be covered with a high dose and the normal tissue is spared to a maximum.

4.3 Treatment Planning

Treatment planning for ion therapy is a multilayered challenge. Initially, it is similar to conventional photon therapy: the tumor is localized based on CT (computerised X-ray tomography) and possibly additional MRI (Magnetic Resonance Imaging) and PET (positron emission tomography) images. The target volume to be treated, as well as the critical structures to be spared,

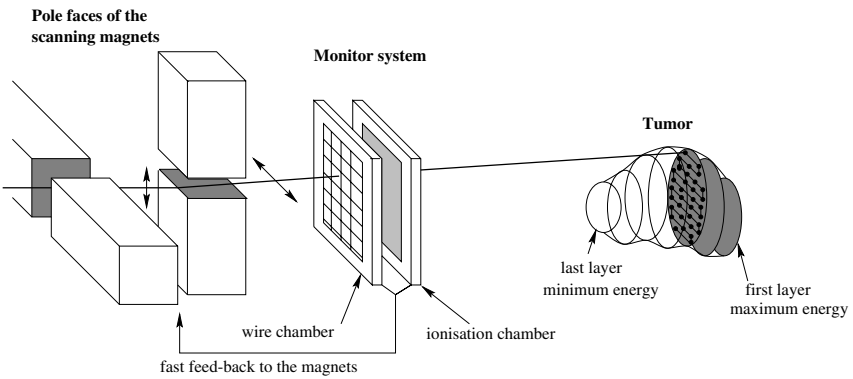

Fig. 14. Schematic drawing of the intensity-controlled rasterscan. The target volume is dissected into layers of equal particle range that are covered by a grid of pixels.

are marked by the physician for each slice of the tomogram. The task of the treatment planner is now to determine the appropriate particle energies, positions and fluences in order to achieve the prescribed dose in a given target volume. As this is done by superposition of many narrow pencil beams, the energy and LET of the primary particle has to be known for every point as well as the number, energy and LET values of the different fragments that contribute to the dose. In the next step the RBE has to be included iteratively for every irradiation point. Due to the complex dependencies from all factors mentioned in the chapter before, this is the most time consuming part of the planning. At GSI these calculations are done using the standard treatment planning software TRiP98 [43–46]. It includes a physical model to describe depth dose profile and nuclear fragmentation of pencil beams of ^{12}C ions, and it also includes the radiobiological model LEM, which allows the calculation of the biologically effective dose, RBE and cell survival (or other biological endpoints) for any dose level and radiation field composition, provided the photon sensitivity for the tissue under consideration is known [37].

4.4 In Vivo Dose Localisation by PET

As can be seen from the Bethe-Bloch-formula, the energy loss, and hence the range of the particle, strongly depends on the density of the target material. For the human body as target with its large variety in density from bones, muscles and fat to air-filled cavities like those in ear and brain, this means that the calculation of the projectile range is a critical point in treatment planning and a direct measurement of the beam distribution inside the patient would be helpful. Here an enormous potential for quality control arises from nuclear fragmentation, which by far compensates for the disadvantages discussed in Sect. 2.4. The stripping of one or two neutrons from the projectile ^{12}C yields the positron emitting isotopes ^{11}C and ^{10}C with half-lifes of 20 min and 19 sec, respectively (Fig. 15). The stopping point of these isotopes can be monitored by measuring the coincident emission of the two annihilation gamma quanta following the positron decay.

The range of the isotopes is only slightly shorter than that of the primary particle, the range relation given approximately by

$$R \sim \frac{A}{Z^2} \qquad R(^{11}C) = \frac{11}{12} R(^{12}C) \; . \tag{9}$$

Thus, from the measured distribution of the annihilation quanta, the range of the stopping particles can be controlled and compared to the calculated range in treatment planning. As there are also positrons emitted from activated target atoms (^{15}O is also produced besides carbon), the dose cannot unambiguously be derived from the measured emitter distribution. Instead, the measured positron distribution has to be compared to an expected distribution that has been calculated before [47,48].

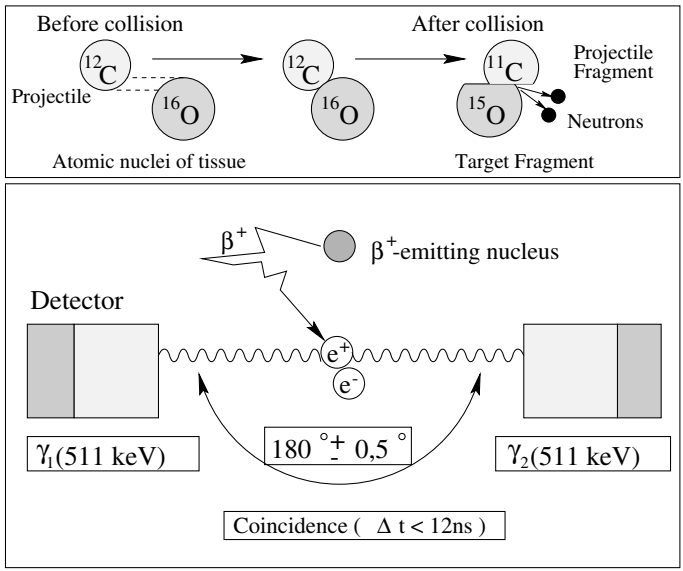

Fig. 15. The stripping of a neutron converts the stable projectile ^{12}C and the stable target atom ^{16}O into the positron-emitting isotopes ^{11}C and ^{15}O. The measurement of the coincident emission of the two annihilation quanta yields a picture, that allows to monitor the stopping point of the incident particles.

4.5 Patient Treatment

The use of accelerated ions for radiotherapy was first started at the Lawrence Berkeley Laboratory (LBL). There the first treatment with protons was done in 1954. Irradiation with helium and heavier ions up to argon on a variety of tumors followed. The Berkeley experience, together with radiobiological experiments, led to the decision to use carbon ions when the first heavy-ion accelerator dedicated solely to therapy began treatment in 1994 at the HIMAC facility in Chiba (Japan). To date, more than 1000 patients and a large variety of tumor sites have been treated.

When GSI began patient irradiation in December 1997, the goal was to demonstrate the clinical feasibility and reliability of newly developed techniques in a small experimental set-up. Active energy variation, intensity-controlled raster scanning and a 3-dimensional biology-based treatment planning offered a new dimension of tumorconform treatment while the on-line PET control set a new safety mark. In this experimental facility, the beam can be used in three blocks of one month per year. Approximately 12 patients per block can be treated with 18 - 20 daily fractions of 3 Gray equivalent and at least two fields per fraction. More than 200 patients have been treated up to now and promising first results are reported [49,50].

The study mainly comprises patients with several types of skull base tumors which are radioresistant against conventional photon irradiation. For

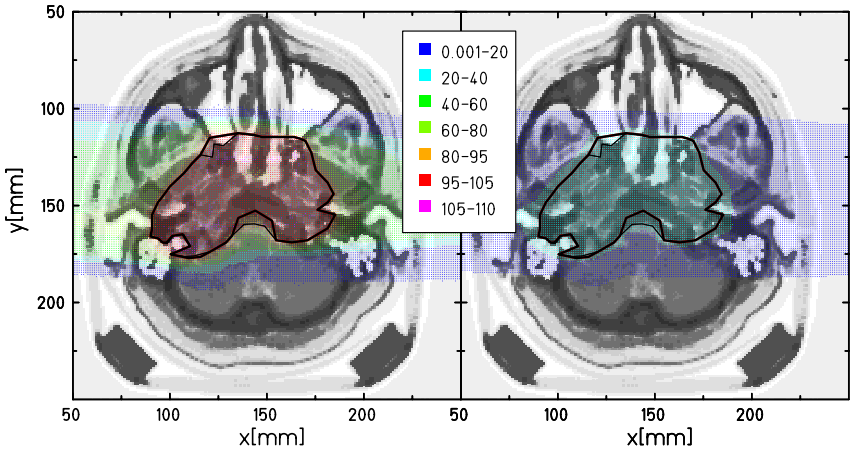

Fig. 16. Computertomography section through the head of a patient. The black line shows the outline of the tumor. The treatment plan is overlayed, showing isodose areas for the physical dose (right) and the biological effective dose (left).(Courtesy of Michael Krämer)

these tumors a total surgical resection is often not feasible and high-dose postoperative radiation therapy is necessary. As in conventional therapy a sufficiently high dose often cannot be safely delivered due to the tolerance doses of neighboring radiosensitive structures (e.g. brainstem, cerebral nerves, eyes), carbon ion therapy represents a promising tool for the management of these tumors. Figure 16 shows a patient example. The figure demonstrates the great difference in physical and biological effective dose, and it shows that the high dose can be restricted to the tumor, sparing sensitive organs like brain stem and optic nerves.

For two types of these tumors, scull base chordomas and low grade chondrosarcomas, the patient recruitment for a clinical phase II study has already been completed. Control rates at four years were 87% for chordomas and 100% for chondrosarcomas, respectively. No local recurrence within the treated volume was observed in any of the patients, indicating that the used RBE values are correct. Irradiation was well tolerated by all patients and no severe toxicity was seen.

The next step, a phase I/II study for the treatment of sacral or spinal chordomas and low grade chondrosarcomas, has been started. They obtained fractionated carbon irradiation in 20 consecutive days with a daily dose of 3.0 GyE, resulting in a median total dose of 60 GyE. Initial results after treatment of 37 patients with chordomas and low grade chondrosarcomas suggest carbon ions as a very promising tool for these tumor types [50]. Patients with other histologies underwent irradiation with a carbon ion boost of 15/18 GyE given in single doses of 3.0 GyE delivered to the macroscopic

tumor after fractionated stereostatic radiotherapy. Median total dose applied in these patients was 63 GyE.

A small group of patients already had conventional radiotherapy and carbon radiotherapy with palliative intent was applied with reduced total dose.

After treatment all patients took part in a prospective follow-up program. The mean follow up was 15 month. The one-year local control rate was 94% in all patients. Though it is still too early to give definitive clinical results, it can be stated, that the clinical effectiveness as well as the technical feasibility of this new therapy modality could clearly be demonstrated.

The next step will be a clinical investigation in a phase III trial in a dedicated facility with a capacity to treat high patient numbers in a clinical environment.

4.6 Planned Facilities

The clinical efficacy and safety of the active beam application system by scanning has been demonstrated. The high local control rates and the low toxicity, that have been seen up to now encourage the future use for a broader group of patients. Thus the realization of dedicated hospital based facilities will be the logical next step. Beside the two Japanese facilities, the HIMAC at Chiba that started in 1994 and Hyogo that started in 2001, there are several strong initiatives for heavy-ion therapy in Europe: the project in Heidelberg that is going to start in 2006 with patient treatment, and several other projects like med-Austron in Austria, TERA in Italy and Etoile in Lyon, France that have at least partially been funded by their governements.

4.7 Conclusions

Heavy ion tumor therapy is an excellent example of the great advantages arising from the intensive co-operation of people from different scientific fields, in this case from physics, biology, engineering sciences and medicine.

The inverse dose profile and the finite range of particle beams allow a greater tumor dose for light ions (from protons to carbon) than for photons, avoiding a dose limiting toxicity to normal tissue. For carbon ions these excellent physical properties of the beam are complemented by an increase of the biological effectiveness toward the end of the range which potentiates the biological effect to the tumor. The active beam shaping, using the rasterscan system and an active energy variation, together with the biologically based treatment planning allow an extremely target conformal irradiation. In addition, the exact distribution of the physical dose can be verified measuring the positron emitter distribution by PET, giving the physician a new dimension in precision. Thus, basic physical and biological knowledge together with innovative technical ideas has been turned into a powerful instrument for medical use.

Acknowledgements

I want to thank F. Bosch, G. Kraft, M. Krämer, M. Scholz and U. Weber for fruitful discussions and helpful advice. I also would like to thank S. Marchand for his help preparing the illustrations.

References

1. H.D.Kogelnik: Radiotherapy and Oncology **42**, 203-211 (1997)
2. P.Brown: Am. J. Roentgenol. **164**, 237-239 (1995)
3. R.E.Zirkle: Am. J. Cancer **25**, 558-567 (1935)
4. J.H.Lawrence, P.C.Abersold, E.O.Lawrence: Proc. Natl. Acad. Sci. USA **22**, 543-557 (1036)
5. R.S.Stone: Am. J. Roentgenol. **59**, 771-785 (1948)
6. R.R.Wilson: Radiology **47**, 487-491 (1946)
7. C.A.Tobias, H.O.Anger, J.H.Lawrence: Am. J. Roentgenol. **67**, 1-27 (1952)
8. C.A.Tobias, J.E.Roberts, J.H.Lawrence et al.: Peaceful Uses At. Energy **10**, 95-106 (1956)
9. W. Bragg, R.Kleemann: Phil. Mag. **10**, 318-340 (1905)
10. G. Kraft, M. Krämer: Advances in Radiat. Biology **17**, 1-52 (1993)
11. H. Bethe: Ann. Phys. (Leipzig) **5**, 325-400 (1930)
12. F. Bloch: Z. Phys. **81**, 363-376 (1933)
13. F. Bloch: Ann. Phys. (Leipzig) **5**, 285-321 (1933)
14. H.W. Barkas: *Nuclear Research Emulsions Vol. I*, (Academic Press New York and London 1963)
15. T.Schwab: Transport von Schwerionen durch Materie innerhalb ionenoptischer Systeme. GSI Report 91-10, PhD Thesis, Giessen (1991)
16. N. Bohr: Phil. Mag. **30**, 581 (1915)
17. S.P. Ahlen: Rev. Mod. Phys. **52**, (1980)
18. G. Moliére: Z. Naturforschung **3a**, (1948)
19. J. Hüfner: Phys. Reports **125**, (1985)
20. ICRU, The Quality Factor in Radiation Protection, ICRU-Report 40, Int.Commission on Radiation Units and Measurements, Washington 1986
21. J. Heilmann, G. Taucher-Scholz et al.: Int. J. Radiat. Oncol. Biol. Phys. **34**, 599-608 (1996)
22. B. Jakob, M. Scholz and G. Taucher-Scholz: Radiat. Res. **154**, 398-405 (2000)
23. M. Belli, R. Cherubini et al.: Int.J.Radiat.Biol. **55**, 93-104 (1989)
24. M. Belli, F. Cera et al.: Int.J.Radiat.Biol **74**, 501-509 (1998)
25. G.W. Barendsen, H.M.D. Walter et al.: Radiat.Res. **18**, 106-119 (1963)
26. G. Kraft: Nucl. Sci. Appl., **3**, 1-28 (1987)
27. L.G. Gerweck and S.V. Kozin: Radiother.Oncol. **50** 135-142, (1999)
28. W.K. Weyrather, S. Ritter et al.: Int.J.Radiat.Biol., **75**, 1357-1364 (1999)
29. M. Suzuki, Y. Kase et al.: Int J Radiat Oncol Biol Phys **48**, 241-250 (2000)
30. W.K. Weyrather: 'Radiobiological Research for Hadron Therapy' In: *Progress in Radio-Oncology VII* Eds. HD Kogelnik, P Lukas, F Sedlmayer (Monduzzi Editore) Bologna, 353-360 (2002)
31. E.J.Hall: *Radiobiology for the Radiologist*, 4th edn. (J.B.Lippincott Company, Philadelphia 1994)

32. E.A. Blakely: 'Biology of BEVALAC beams' In: *Pion and heavy ion Radiotherapy: Pre-Clinical and Clinical Studies* Skarsgard LD Ed. New York. (Elsevier Science Publishing Co, Inc.) 229-250 (1982)
33. Z. Han, H. Suzuki et al.: Adv. Space Res. **22**, 1725-1732 (1998)
34. J. Kiefer, P. Schmidt and S. Koch: Radiat.Res. **156**, 607-611 (2001)
35. Y. Furusawa, K. Fukutsu et al.: Radiat.Res. **154**, 485-496 (2000)
36. O. Jäkel and M. Krämer: Physica Medica Vol XIV/1, 53-62 (1998)
37. M. Scholz, A.M. Kellerer et al.: Radiat.Environ.Biophys. **36**, 59-66 (1997)
38. M. Scholz: Bull Cancer, **83**, 50s - 54s (1996)
39. T. Zacharias, W. Dörr et al.: Acta Oncologica **36**, (1997)
40. M. Scholz and G. Kraft: Radiat. Prot. Dosimetry **52** 29-33, (1994)
41. G. Kraft: Progress in Particle and Nuclear Physics **45**, S473 - S 544, (2000)
42. Th. Haberer, W. Becher et al.: Nucl. Instr. and Meth. in Phys. Res. **A330**, 296-305 (1993)
43. M. Krämer, O. Jäkel et al.: PMB **45/11**, 3299-3317 (2000)
44. M. Krämer and M. Scholz: PMB **45/11**, 3319-3330 (2000)
45. O. Jäkel, M. Krämer et al.: PMB
46. M. Krämer: J. Radiat. Res. **42**, 39-46 (2001) **46/4**, 1101-1116 (2001)
47. W. Enghardt et al.: Proc. Int. Conf. on Biological Applications of Relativistic Nuclei, Clermont-Ferrand, France, Oct. 1992, 30
48. W. Enghardt, J. Debus et al.: Strahlenther. Onkol., **175**, Suppl. II, 33-36 (1999)
49. J. Debus, T. Haberer et al.: Strahlenther. Onkol. **176**, 211 - 216 (2000)
50. D. Schulz-Ertner, T. Haberer et al.: Int J Radiat Oncol Biol Phys **53**, 36-42 (2002)